





## Multiscale perspective on wetting on switchable substrates: Mapping between microscopic and mesoscopic models

Moritz Stieneker <sup>1,2,\*</sup> Leon Topp <sup>3,\*</sup> Svetlana V. Gurevich <sup>1,2,4,†</sup> and Andreas Heuer <sup>3,2,4,‡</sup>

<sup>1</sup>University of Münster, Institute for Theoretical Physics, Wilhelm-Klemm-Str. 9, 48149 Münster, Germany

<sup>2</sup>University of Münster, Center for Nonlinear Science (CeNoS), Corrensstr. 2, 48149 Münster, Germany

<sup>3</sup>University of Münster, Institute for Physical Chemistry, Corrensstr. 28/30, 48149 Münster, Germany

<sup>4</sup>University of Münster, Center for Multiscale Theory and Computation (CMTc), Corrensstr. 40, 48149 Münster, Germany



(Received 25 November 2021; accepted 15 December 2022; published 18 January 2023)

To understand the nonequilibrium relaxation dynamics of a liquid droplet on a switchable substrate, the interplay of different length and timescales needs to be understood. We present a method to map the microscopic information from a molecular-dynamics simulation to a mesoscopic scale, reflected by a thin-film model. After a discussion of the mapping procedure, we first analyze the relaxation of a liquid droplet upon switching the wettability of the substrate. Furthermore, we show that a nearly identical mapping procedure can be used to describe two coalescing droplets. With our procedure we take a first step to extend the mapping from the equilibrium case to nonequilibrium wetting dynamics, thus allowing for quantitative multiscale analysis.

DOI: [10.1103/PhysRevFluids.8.013902](https://doi.org/10.1103/PhysRevFluids.8.013902)

### I. INTRODUCTION

Finding ways to manipulate and control patterns of liquids has been the goal of scientists for a long time. Back in 1992, Chaudhury and Whitesides were able to exploit a wettability gradient to make a droplet walk up an incline [1]. Another example includes extensive experimental studies of the instabilities, dynamics, and morphological transitions of patterns in thin liquid films on different prestructured substrates, see, e.g., Refs. [2–6]. Nowadays, such systems can also be examined theoretically on different length- and timescales [7–12], e.g., transversal instabilities of ridges on prestructured substrates have been studied with a combination of a microscopic kinetic Monte Carlo model and a continuum thin-film model [13–15].

In recent years the development of switchable surfaces gained pace. On such surfaces, the wettability can be varied by applying an external stimulus like a change of the pH value or by illumination with light of a defined wavelength. Prominent examples for such surfaces are inorganic materials like  $\text{TiO}_2$  or  $\text{ZnO}$  [16–18] which have the advantage of a large difference between the contact angles before and after switching. Since the switching process from the hydrophilic to the hydrophobic case for these substrates is rather slow, another class of substrates is of great interest, namely, substrates coated with a self-assembled monolayer (SAM) consisting of molecules with azobenzene or other photoresponsive moieties [19–21]. The azobenzene moiety can be switched with UV light from a *trans* to a *cis* state which has a lower wettability while the reverse process can be induced by illumination with blue light. These surfaces adapt much faster at the disadvantage of

\*These authors contributed equally to this work.

†gurevics@uni-muenster.de

‡andheuer@uni-muenster.de

lower contact angle differences. However, in recent years improvements that yield a higher change of the contact angle have been made by microstructuring the surface [22,23].

Switchable substrates promise rich nonequilibrium behavior and an additional mechanism to control pattern formation, which can be employed in addition to static prestructures. In particular, it was demonstrated that it is possible to guide the movement of a droplet reversibly by applying a light gradient [21,24], i.e., changing the wettability close to the droplet. Recent theoretical work by Grawitter and Stark [25] investigated how droplets can be steered with the help of spatiotemporal wettability patterns using the macroscopic boundary element method. This is relevant especially for the development of lab-on-a-chip devices [26].

Theoretical models play a key role to gain an improved understanding of the nonequilibrium behavior on switchable substrates. In particular, to study microscopic phenomena atomistic simulation methods like molecular dynamics (MD) have become an established approach [27–29]. On larger length- and timescales mesoscopic thin-film descriptions have been successfully applied for a variety of different wetting systems, see the reviews [30–32]. While microscopic MD simulations can incorporate more details of the specific interactions between liquid and substrate, continuum mesoscopic models cannot resolve microscopic details but are able to address much larger length and timescales. Furthermore, continuous mesoscopic models allow us to apply the tool kit of bifurcation analysis to investigate instabilities offering analytical insights which are not possible in discrete, microscopic models. Bifurcation analysis combined with parameter sweeps, which are computationally cheaper compared with microscopic models, can then indicate interesting parameter regimes and timescales to analyze in the microscopic model for a more detailed investigation. This helps avoid computational costs for simulations in irrelevant regimes.

Thus, combining different microscopic and continuum descriptions seems natural and has been done by Wu *et al.* [14], among others. There, the spreading dynamics of drops on solid surfaces were investigated by solving the Navier–Stokes equations in a continuum domain comprised of the main body of the drop together with MD simulations in a particle domain in the vicinity of the contact line. Another example of the combination of models across length- and timescales is the work by Zhang *et al.* who combined MD with volume of fluid simulations to study droplet spreading on surfaces [15]. Also, Hadjiconstantinou supplied both a continuum and MD method for the flow of two immiscible fluids in a channel [33]. In Ref. [13] kinetic Monte Carlo simulations and a thin-film continuum model were combined to comparatively study the Plateau-Rayleigh instability of ridges formed on prestructured substrates. It was shown that the evolution of the occurring instability qualitatively agrees between the two models.

Given the advantages and disadvantages of the different methods, it is evident that a mapping between the methods is of great interest. For the static case, various microscopic descriptions have been employed to improve the mesoscopic models mainly by extracting the binding potential (also referred to as the wetting, disjoining, or interface potential) [34,35]. For partially wetting liquids, the interface potential is particularly important for describing the droplets in the vicinity of the three-phase contact line. It is defined as a uniform thickness layer of the liquid on a flat solid wall in the presence of a bulk vapor phase.

In particular, Tretyakov *et al.* extracted properties from a MD model to study equilibrium properties in a continuum model and found quantitative agreements between the MD model and the continuum model [36]. Similar results can be obtained based on density-functional theory [35,37]. The results obtained in Refs. [35,37] could be verified by a different method of extracting the disjoining pressure, namely, using nudged elastic band calculations [38]. Hughes *et al.* could relate oscillatory disjoining pressures to layering effects and found qualitative agreements to profile shapes observed in experiments [35].

However, so far, the focus has been on static equilibrium conditions. As switchable substrates inherently lead to nonequilibrium dynamics, static considerations are not sufficient anymore. Therefore, our focus here is on the mapping of the timescales.

In this paper, we propose a general method to map a MD model to a mesoscopic thin-film model making the first step toward quantitative comparisons of dynamics between models acting

on mesoscopic and microscopic scales. The functional form of the presented mapping can help to understand the differences between the employed models and shed light upon the corresponding timescales and transport quantities. A mapping between the model parameters can possibly provide insights if continuum models are able to grasp all the features present in particle-based, microscopic models.

The paper is structured as follows: In Sec. II we describe setups for MD and TFE simulations. Afterward, in Sec. III A our procedure for the spatial and temporal mapping between MD and TFE simulations is introduced. Two applications—a droplet adapting to a new wettability and the coalescence of two droplets—are shown in Secs. III B and III C. Finally, we conclude our results in Sec. IV.

## II. THEORETICAL BACKGROUND

### A. Molecular-dynamics theory

On the microscopic level, we employ the framework HOOMD [39] to perform simulations of a system consisting of Lennard-Jones particles in a canonical ensemble. All particles in the system are interacting through the Lennard-Jones potential

$$V(r_{lj}) = 4\epsilon_{lj} \left[ \left( \frac{\sigma_{lj}}{r_{lj}} \right)^{12} - \left( \frac{\sigma_{lj}}{r_{lj}} \right)^6 \right], \quad (1)$$

where  $r_{lj}$  is the distance between particles  $l$  and  $j$ ,  $\epsilon_{lj}$  is the interaction strength between the particles, and  $\sigma_{lj} = \frac{1}{2}(\sigma_l + \sigma_j)$  is the mean of the particle diameters  $\sigma_l$  and  $\sigma_j$ . This potential is truncated and shifted at a cut-off radius of  $r_c = 2.5\sigma$ . The interaction strength is calculated as the geometric mean of the self-interaction parameters  $\epsilon_{lj} = \sqrt{\epsilon_l \epsilon_j}$ . We distinguish two types of particles, namely, the substrate particles (here denoted with “ $s$ ”), which are fixed at their positions during the simulation, and the fluid ones (denoted with “ $f$ ”), which form the droplet or are in the gas phase. While the interaction strength of the droplet particles is set to  $\epsilon_f = 1\epsilon$  for all simulations, by varying the parameter  $\epsilon_s$  the wettability of the surface can be changed. Note that  $\epsilon_w = \sqrt{\epsilon_s \epsilon_f} = \sqrt{\epsilon_s}$  denotes the interaction strength between a fluid and substrate particles because we set  $\epsilon_f = 1\epsilon$ . In all simulations, we vary the value  $\epsilon_w$  between  $\epsilon_{\text{HW}} = 0.762\epsilon$  for a high wettability and  $\epsilon_{\text{LW}} = 0.632\epsilon$  for a low wettability if not denoted otherwise. The particle diameter is set to  $\sigma_f = \sigma_s = \sigma$  for the solid as well as for the fluid particles. The reduced time unit is set to  $\tau = \sigma \sqrt{M/\epsilon}/200$ , where  $M$  is the particle mass and the reduced temperature is  $\frac{k_B T}{\epsilon} = 0.75$ . The substrate particles are arrayed in two layers of a fcc(111) lattice. To exclude the effect of line tension we consider cylindrically shaped droplets as can be seen in Fig. 1. In the  $y$  direction our domain is  $48.6\sigma$  wide. We performed simulations with an approximately 40% wider and 40% smaller domain in  $y$  direction which show practically identical results to confirm that the width is large enough to neglect finite-size effects and small enough to suppress Plateau-Rayleigh instabilities. The total amount of fluid particles is set to  $N = 4 \times 10^4$  per droplet. To control the temperature we use a dissipative particle dynamics (DPD) thermostat [40,41] to reproduce the correct hydrodynamics. In addition, we averaged every simulation setup over 50 trajectories to generate sufficient statistics.

To analyze the trajectories of the particles we first perform a projection along the  $y$  axis so that we effectively analyze a two-dimensional (2D) system (with axes  $x$  and  $z$  cf. Figure 1). A common procedure [42–44] to extract the droplet shapes from these projections is to calculate the density field first and then determine the position of the liquid-gas interface for different heights  $z$ . Thus, we calculate the position of the liquid-vapor interface for every  $z$  position by fitting the density with the function

$$c_z(x) = \frac{1}{2}(c_l + c_g) - \frac{1}{2}(c_l - c_g) \tanh \left( \frac{2[x - x_\beta(z)]}{d_\beta} \right). \quad (2)$$

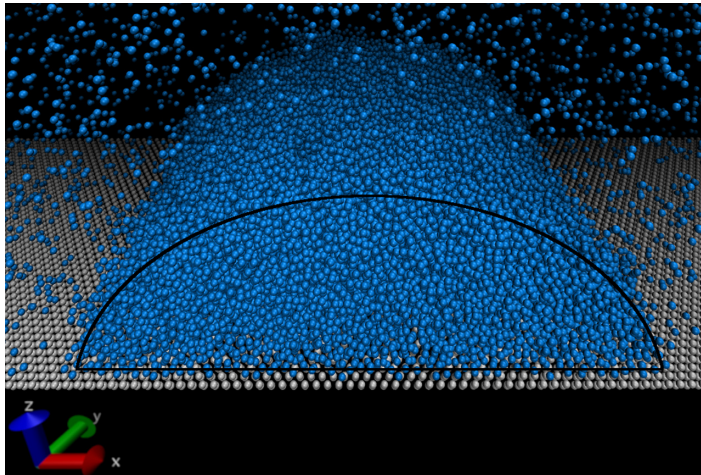


FIG. 1. Snapshot from a MD simulation showing fluid particles (blue) forming a cylindrically shaped droplet placed on two layers of a fcc(111) surface.

Here,  $c(x)$ ,  $c_l$ , and  $c_g$  are the particle density at position  $x$ , the density in the bulk, and the density in the gas phase, respectively.  $x_\beta(z)$  gives the position of the liquid-vapor transition by using a crossing criterion. The parameter  $d_\beta$  determines the width of the liquid-vapor interface. The same procedure can be applied for the perpendicular direction parallel to the  $z$  axis to compute the liquid-gas interface position  $z_\beta$  for a given  $x$  position. For our analysis, we used the values of  $x_\beta(z)$  for  $z < h/2$  with a bin size of  $1\sigma$  to average out layering effects and the values of  $z_\beta(x)$  for  $z > h/2$  where we use a bin size of  $0.1\sigma$ . Here,  $h$  is the height of the droplet. Both methods can be consistently combined (cf. details in the Supplemental Material [45]) and help to resolve the droplet peaks better because all relevant fits are along lines with a significant share of particles in the liquid phase. Finally, we have chosen the height of the upper layer of the substrate to be at  $z = -0.5\sigma$  since the particles have a diameter of  $\sigma$ , i.e., the top of the substrate particle is at  $z = 0\sigma$ .

### B. Thin-film equation theory

The mesoscopic continuum model employed in this paper is based on the thin-film or lubrication approximation for the Navier–Stokes equation [30]. The lubrication approximation is given by an evolution equation of the local height  $h = h(x, y, t)$ , which can be written in a gradient dynamics form as [32,46]

$$\partial_t h = \nabla \cdot \left[ M(h) \nabla \frac{\delta \mathcal{F}}{\delta h} \right], \quad (3)$$

with the mobility  $M(h)$  and the free-energy functional  $\mathcal{F} = \mathcal{F}[h]$ . Here, we assume no-slip boundary conditions at the substrate leading to a mobility of  $M(h) = h^3/(3\eta)$  with the dynamic viscosity  $\eta$  [30]. Several slip regimes can be accounted for by different choices for  $M(h)$  [47]. For a discussion of the influence of the mobility on the dynamics cf. Refs. [11,48]. The generalized pressure  $P = \frac{\delta \mathcal{F}}{\delta h}$  is given by

$$P(h, x, t) = -\gamma \Delta h - \Pi(h, t), \quad (4)$$

with the surface tension  $\gamma$  and the disjoining pressure  $\Pi(h, t)$ . The latter is chosen as

$$\Pi(h, t) = \left( \frac{B}{h^6} - \frac{A}{h^3} \right) [1 + \rho(t)]. \quad (5)$$

Here,  $A$  and  $B$  denote the interaction strengths of long- and short-range forces, respectively, where  $A$  is directly connected to the Hamaker constant  $H$  by  $A = H/6\pi$ . A different choice of the disjoining pressure is possible, see, e.g., Refs. [30,34,46] for details. Even though the disjoining pressure determines mainly equilibrium properties, an effect on dynamics is possible, because nonequilibrium transient states are inherently involved in dynamics. In the present paper, the disjoining pressure in Eq. (5) is modulated by the parameter  $\rho = \rho(t)$  to model switchable substrates, where  $\rho$  is a parameter corresponding to the wettability contrast. The use of the no-slip boundary condition at the substrate leads to a logarithmic energy dissipation at the contact line [31]. This singularity can be resolved by introducing a precursor film  $h = h_p$  [30,31], which is also present on macroscopically “dry” parts of the substrate. Alternate ways to resolve the singularity problem at the contact line are presented by Bonn *et al.* [31]. Note that a temporal modulation of the disjoining pressure as shown in Eq. (5) does not change the precursor film height [11,13].

In the following, we employ the nondimensionalized form of Eq. (3), where  $h$ ,  $x$ , and  $t$  are scaled in such a way, that  $3\eta$ ,  $\gamma$ ,  $A$ , and  $B$  are incorporated in the corresponding scaling (a detailed derivation of the nondimensionalization is presented in the Supplemental Material [45]). This leads to the evolution equation

$$\partial_t h = \nabla \cdot \left\{ h^3 \nabla \left[ -\Delta h - \frac{5}{3} \Theta_{\text{eq}}^2 \chi^2 \left( \frac{\chi^3}{h^6} - \frac{1}{h^3} \right) [1 + \rho(t)] \right] \right\}, \quad (6)$$

with the equilibrium contact angle  $\Theta_{\text{eq}}$  and the parameter  $\chi = h_p/h_0$ , where  $h_0$  is the spatial scale. For further analysis, we subtract the precursor film height  $h_p$  from the film height  $h$  in Eq. (6). Additionally, we keep  $\Theta_{\text{eq}} = \sqrt{3/5}$  so that the effective equilibrium contact angle  $\tilde{\Theta}_{\text{eq}}$  is determined by the parameter  $\rho$  as

$$\tilde{\Theta}_{\text{eq}} = \Theta_{\text{eq}} \sqrt{1 + \rho(t)}. \quad (7)$$

In the MD model, there is no equivalent precursor film, so  $\chi$  has to be chosen small. We use a value of  $\chi = 0.01$  in the following because smaller values of  $\chi$  do not change the contact region significantly and would lead to increased computational efforts and possible numerical problems. Note that for different values of  $\rho$  the ratio of the precursor film height  $h_p$  to the maximum droplet height  $h_{\text{max}}$  does change for constant volume.

It should be noted that temperature does not enter directly into the TFE model (6). However, indirectly the temperature enters the TFE model through the surface tension  $\gamma$ , the viscosity  $\eta$  and the particular shape of the disjoining pressure, which determines the wetting regime. In particular, the minimum of the interface potential (the integral of the disjoining pressure) is directly connected to the contact angle in the mesoscopic picture as a known disjoining pressure is sufficient to determine the equilibrium state [11,31]. Direct temperature dependence can be incorporated in thin-film models, e.g., Davidovitch *et al.* have shown that higher temperatures leads to faster spreading [49]. In our case, this would be included via a lower viscosity.

The direct numerical simulations within the TFE model (6) are based on the finite-element library oomph-lib [50]. In contrast to the MD model, cylindrically shaped droplets can directly be simulated on a one-dimensional (1D) domain in the thin-film model, which reduces the spatial dimension of the problem by one and directly excludes any instabilities possibly occurring in the transversal  $y$  direction. In general, one can plug profiles from the MD model into the TFE model. As the MD model exhibits noise, this requires small time steps in the simulation to reach a smooth profile. In some circumstances, the time steps in the employed adaptive time stepping algorithm can get so small, that rounding errors of the machine can influence the results. To avoid such behavior, we



apply a filter to the MD data before we start the simulation in the TFE model. Details on the applied LOWESS filter can be found in the Supplemental Material [45].

### III. RESULTS

#### A. How to compare scales

To compare the scales in the case of a static droplet, a mapping between  $\epsilon_w$  and  $\rho$  responsible for the wettability in their respective models is necessary. For dynamic comparisons, the timescales need to be mapped as well. In the first part of this section, we describe the mapping in the static, equilibrium case. In the second part, we describe the mapping of the timescales.

The relation of the liquid-solid interaction strength to the contact angle has been the focus of research for quite some time, e.g., Sullivan [51] came up with a qualitative theory based on a van der Waals model in 1981. This is closely related to the research on wetting transitions substantially advanced by Refs. [52–55]. Pandit *et al.* [52] investigated the wetting transition within a lattice-gas model for different interaction strengths and interaction ranges. Within the framework of a systematic van der Waals theory (mean-field model), critical wetting can also be observed [53]. Such critical wetting is nongeneric as shown first by Dietrich and Schick [54].

Despite the efforts in this field, there is no way to compute the relation between the interaction strength  $\epsilon_w$  and the wettability parameter  $\rho$  without doing involved numerics. Even if possible, theories often only promise qualitative agreements [51], which is insufficient for our aim of a quantitative agreement in the dynamics of microscopic and mesoscopic models.

For an even better agreement of the equilibrium droplet shapes, one could try to extract the exact shape of the disjoining pressure  $\Pi$ . As mentioned above, the disjoining potential can in principle be extracted from MD simulations, lattice density-functional theory (DFT), and continuum DFT [35–38]. However, the extraction of wetting potential is tricky and some open questions remain [38].

Here we choose a different approach and map the interaction strength  $\epsilon_w$  from the MD model to the parameter  $\rho$  from the TFE model so that according to an appropriate criterion both models show the same droplet shape. Since the volume is fixed, the shape of the static droplet is characterized by just one parameter such as the height or the contact angle. As a consequence,  $\rho$  is used for a reliable, yet, empirical static mapping. This allows us to take the next step of a quantitative comparison not only of statics but also of dynamics.

Contact angles are hard to define and measure consistently in microscopic and mesoscopic models. The definition of the contact angle can have a strong influence and at the nanoscale the contact angle can depend on the droplet size [56]. Indeed, in the mesoscopic TFE model the contact region is not represented accurately due to the lubrication approximation [31] and the contact line is hard to define due to the necessarily smooth transition to the precursor film. Consequently, it is not clear how results based on a contact angle mapping can be interpreted reliably. Figure 2 shows two mapped equilibrium profiles based on our mapping described in the following to give an idea, of how the lubrication approximation (blue curve) influences equilibrium droplet shapes in the contact region.

Instead, we introduce *the relative full width at half maximum* (rFWHM), which is defined as the height of the droplet divided by its width at half of the height. This parameter is not sensitive to the droplet shape in the contact region while being sensitive to the overall shape. The measure rFWHM can be regarded as a computationally cheap way to estimate the curvature and thus is closely related to the contact angle. Another advantage of the rFWHM is that one can straightforwardly analyze the temporal evolution. If one measures the contact angle by fitting the droplet shape with a circular cap, the quality of the fit varies, because dynamic droplets do not necessarily have a circular cap shape and thus the error margin of the measured contact angle changes.

We computed the equilibrium droplet shapes in both models and measured rFWHM in dependence of  $\epsilon_w$  for the MD model and as a function of  $\rho$  for the TFE model. The rFWHM shows

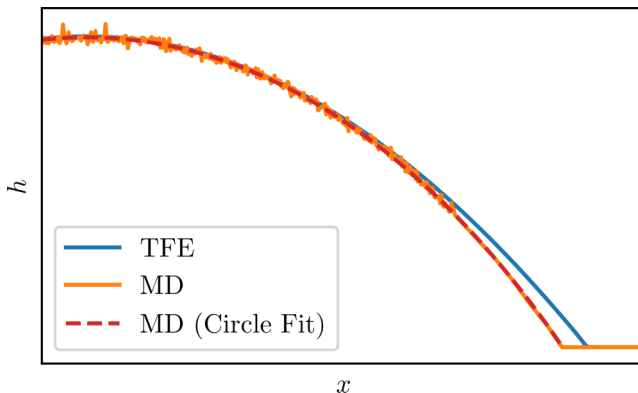


FIG. 2. Spatially rescaled height profiles of a static droplet from the MD and TFE model corresponding to  $\epsilon_w = 0.762$  and a circle fit to the height profile from the MD model.

an approximately linear dependence of the interaction parameter squared  $\epsilon_w^2$  so that we employed a linear fit to avoid a computationally costly parameter sweep with a higher resolution in  $\epsilon_w$ . The low computational cost in the TFE model makes a detailed parameter sweep possible so that linear interpolation can be used to compute the rFWHM for arbitrary values of  $\rho$  and vice versa. Combining both results yields a reliable, numerical mapping between  $\epsilon_w$  and  $\rho$  as can be seen in Fig. 3. Additionally, Fig. 3 shows the mapping for different reduced temperatures. At higher temperatures, a defined interaction strength  $\epsilon_w$  is mapped to a lower value of  $\rho$ , which corresponds to a lower contact angle. This explains how the disjoining pressure can capture the temperature dependence implicitly in the TFE model.

For the mapping of the spatial scales, the  $x$  and  $z$  coordinates can be simply normalized with the maximum height  $h_{\text{ref}}$  of the droplet in the corresponding model at a certain wettability. Here, the maximum height of a droplet on a surface with a wettability corresponding to  $\epsilon_w = 0.632 \epsilon$  in both models is used to scale the film height and the  $x$  coordinates ( $h_{\text{ref}} = x_{\text{ref}}$ ). In principle, the scaling height can be chosen arbitrarily as long as it corresponds to the same height in both models, i.e. droplet height at a certain wettability.

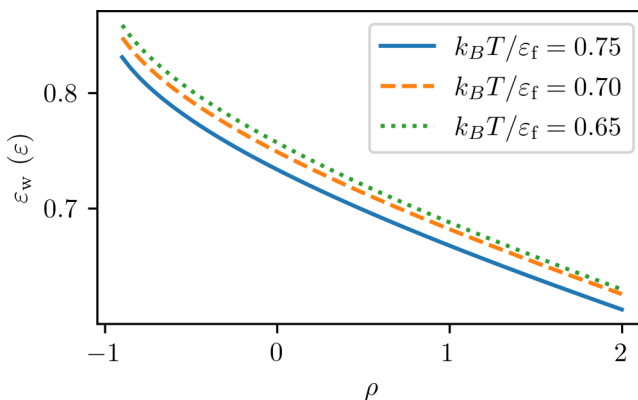


FIG. 3. Resulting mapping from the parameter  $\rho$  modulating the disjoining pressure in the thin-film picture to the interaction strength between solid and liquid  $\epsilon_w$  in the MD model. The mapping is shown for multiple reduced temperatures.  $k_B T / \epsilon = 0.75$  is the value used for all the simulations within this paper.

A comparison of static droplet shapes from both models can be seen in Fig. 2. Both profiles match well for heights of  $h > 0.4 h_{\max}$ . As anticipated, there is some deviation in the contact region due to the lubrication approximation in the TFE model.

The mobility  $M$  is particularly important for the dynamics, as it influences the pathway towards the minimum of the free energy [11]. We use a cubic mobility stemming from the no-slip boundary condition. Other choices are possible, e.g., to respect slip at the substrate [57].

To achieve a rather generic approach we compute the deviation  $\Delta = |K_{\text{MD}} - K_{\text{TFE}}|$  of a measure  $K$  from the TFE profiles for every MD time step first which is defined as

$$K = \frac{\int_{h>0.4h_{\max}} x^2 h \, dx}{\left( \int_{h>0.4h_{\max}} h \, dx \right)^2}. \quad (8)$$

An advantage of this choice of  $K$  is that it could be applied to different cases like a droplet adapting to a new surface wettability or the coalescence of two droplets as shown later. This is not possible by taking a measure as the rFWHM because it is only defined for a single droplet. Note that it is possible to calculate the rFWHM from  $K$  in the case  $K$  is calculated for a system with a single droplet with the numerically obtained formula (details are given in the Supplemental Material [45])

$$\text{rFWHM} = \frac{1}{0.0614 + 10.92K}. \quad (9)$$

To exclude systematic errors originating from the lubrication approximation and its effect on the contact region we only consider regions with  $h > 0.4 h_{\max}$ . Note that the threshold value  $0.4 h_{\max}$  only has a small influence as long as the major part of the contact region is not accounted for.

Physically  $K$  can be understood as a measure of the variance or spread of the liquid. However, the physical interpretation is not relevant for the mapping and  $K$  can be substituted by any measure with monotonic evolution for the situation under investigation.

Since we are interested especially in a mapping of the dynamics we furthermore use a version of  $K_{\text{MD}}$  and  $K_{\text{TF}}$  that is normalized between 0 and 1 to compensate for small differences of  $K$  present in the static droplet profiles. Such small errors would propagate to the dynamic mapping. The normalized  $K$  is defined as

$$K_{\text{norm}} = \frac{K - K(t=0)}{K(t=\infty) - K(t=0)}. \quad (10)$$

With the help of the computed deviations, we can match every time step in the MD simulation to the time step of the TFE simulation with the least amount of deviation. This results in a mapping  $t_{\text{MD}} \mapsto t_{\text{TFE}}$ . The mapping in this direction is more convenient as the MD model is a first-principle model and uses a constant time step in contrast to the TFE model.

In the following, we apply the resulting mapping to two different cases to demonstrate its applicability. First, we investigate the mapping for a liquid ridge placed on a homogeneous, switchable substrate and, second, we consider the mapping in the case of coalescence of two ridges. There we show that our mapping method can be applied universally and does not require additional simulations or measurements, where one had to worry about initial conditions influencing the measurement of a characteristic time.

### B. Single switch on a homogeneous substrate

As a first example of the mapping procedure presented in Sec. III A we applied it to the dynamics of a one-dimensional ridge on a switchable substrate. The procedure for the simulations is as follows: The ridge is equilibrated at either high or low wettability ( $\epsilon_{\text{HW}} = 0.762 \epsilon$  and  $\epsilon_{\text{LW}} =$



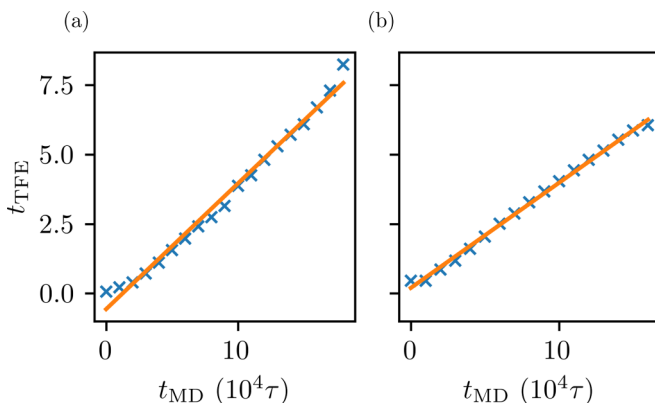


FIG. 4. Result of the mapping approach applied to (a) the switching from  $\epsilon_{\text{LW}}$  to  $\epsilon_{\text{HW}}$  (blue data points and orange linear fit) and (b) from  $\epsilon_{\text{HW}}$  to  $\epsilon_{\text{LW}}$ .

0.632  $\epsilon$ , respectively) before the wettability is instantaneously switched to the other wettability at  $t = 0$ .

Figures 4(a) and 4(b) show the results of the mapping approach for switching towards higher and lower wettability, respectively. In both cases, the data points of the mapping hardly deviate from a linear fit.

Only the first two matched time steps deviate from the linear fit. This is possibly due to initial inertial effects in the MD model, which are not present in the TFE model [30,31]. Consequently, a linear fit of the mapping does not go directly through the origin. As expected, deviations between the MD model and the TFE model exist in the contact region, corresponding to regions of the droplets with small heights. As a consequence, the mapping is becoming worse for very high wettabilities because the contact region is more extended. A cutoff for large times needs to be introduced because eventually changes in the droplet profile between time steps are dominated by noise in the MD model and matched times are not meaningful anymore.

The space-time representations in Fig. 5 show the evolution of the film profile  $h(x, t)$  as the ridge adapts to the new wettability. The color map indicates the film's height. The results from both models look very similar in this representation. Besides the noise in the MD model, the offset for the switch towards higher wettability accounts for the only general difference. This offset is a consequence of the previously described effect of the initial assimilation. To better grasp how well the models compare, the change of the height in time at three distinct points in space is shown in Fig. 6. For the direct comparison between the models times from the TFE model are converted into MD units  $\tau$ .

For both switching directions, the evolution of the height at points I and II is in close agreement between the models. The situation is however a bit different for point III. Only for maximum profile heights reached at this position the agreement is close. For smaller heights, however, one can see differences. This behavior can easily be explained since already static ridges from both models do not match well in the region located close to the contact line (cf. Fig. 2). The reason is the underlying lubrication approximation in the TFE model, which results in higher film heights in the contact region compared with the MD model.

One can also find a position, where the height profile behaves nonmonotonically. In particular, for point II the film height increases first and then decreases to its equilibrium value. This effect occurs for both switching directions, although it is more pronounced when switching from high to low wettability. The dotted black lines in Fig. 6 are a guide to the eye to better see the nonmonotonic behavior. In general, it is not surprising to find this nonmonotonic behavior since this occurs also in the Gaussian solution of the heat equation or Fick's second law. However, finding such a distinct

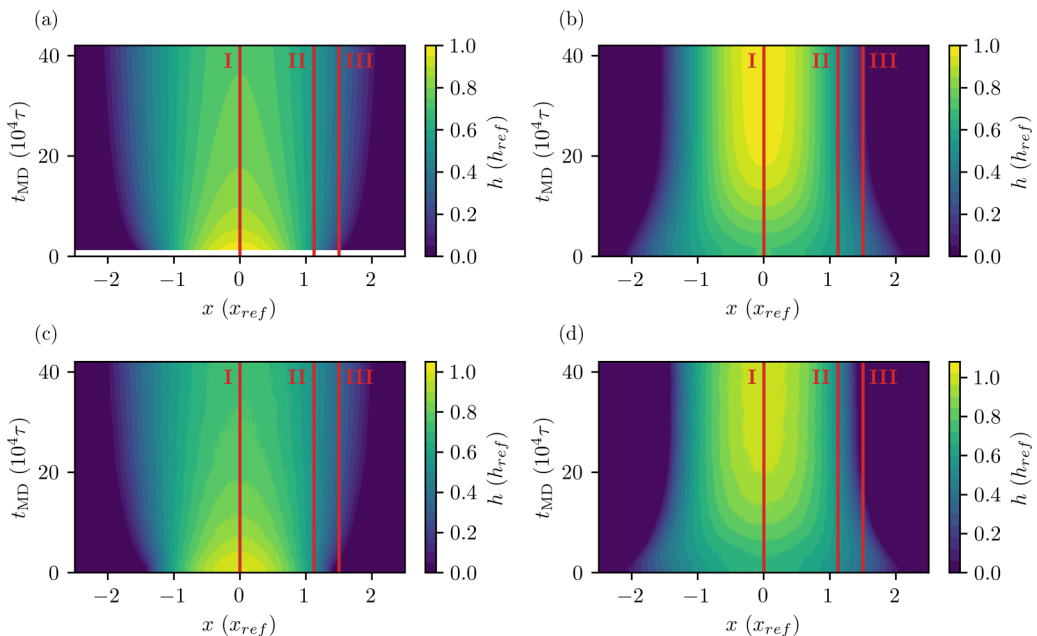


FIG. 5. Space-time plots showing the evolution of the height profile after a change in wettability for  $\epsilon_{\text{HW}} = 0.762 \epsilon$  and  $\epsilon_{\text{LW}} = 0.632 \epsilon$ . Panels (a) and (c) switch from low to high wettability in the TFE and the MD model, respectively. Panels (b) and (d) show inverse switching directions in the TFE and the MD model, respectively. Red vertical lines labeled I, II, and III indicate at which positions the height profile evolution is shown in Fig. 6.

behavior in both models confirms that the parameters are chosen in such a way, that both models show consistent behavior, as this behavior could also be present at a different film height, a different position or a different point in time.

Table I shows resulting timescale ratios (corresponding to the slope of the linear fit) for the switching process between different wettabilities. Note that the value of  $R$ , in general, could depend on the initial and the final wettability. The data in Table I does not indicate that there is a dependence

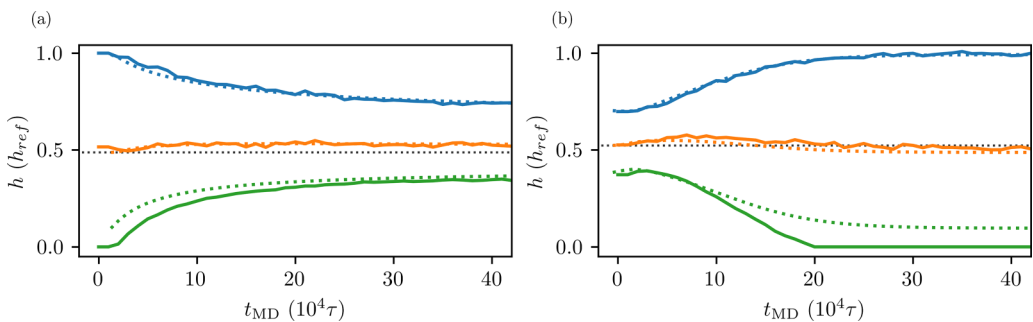


FIG. 6. Three characteristic height profiles along the marked lines I (blue), II (orange), and III (red) as shown in Figure 5. The height profiles extracted from the MD model are presented with solid lines. The dotted lines are TFE results with the temporal scaling obtained using our mapping approach. The height  $h$  is given relative to the maximum height. The black dotted line indicates the initial height in the TFE model for slice II to emphasize the nonmonotonic behavior for the height profile at this position. (a) The wettability is switched from low to high, (b) the wettability is switched in the opposite direction.

TABLE I. Comparison of timescale ratios for different wettabilities and wettability differences computed with our mapping approach.

$\epsilon_{\text{LW}} [\epsilon]$	$\epsilon_{\text{HW}} [\epsilon]$	$R_{f_{\text{HW} \rightarrow \text{LW}}} [\tau]$	$R_{f_{\text{LW} \rightarrow \text{HW}}} [\tau]$
0.632	0.671	$2.98 \times 10^4$	$2.70 \times 10^4$
0.671	0.707	$2.95 \times 10^4$	$2.45 \times 10^4$
0.707	0.742	$2.13 \times 10^4$	$2.15 \times 10^4$
0.632	0.762	$2.64 \times 10^4$	$2.21 \times 10^4$

on the initial wettability at least not within the error margin. The error margin is approximately 10% if one considers the influence of the cutoff for the fit. Notably, the timescale ratio  $R$  shows a tendency to decrease if the wettability increases. However, the resulting deviations are quite small (less than a factor of two in the considered range of wettabilities). Furthermore, we observe a linear time mapping for all wettabilities. This shows that indeed the droplet evolution, seen in the MD simulations, is well reflected by the TFE.

Note that the magnitude of the scaling factors can be expected by comparing the timescales from TF and MD simulations. Since the timescale of the TFE simulations is  $t_0 = \frac{3\eta h_0}{\gamma}$  (cf. Supplemental Material [45]) this would result in a value of  $t_0 \approx 3.9 \times 10^4 \tau$  by plugging in the values  $h_0 = 14.40 \sigma$  and  $\eta = (2.14 \pm 0.08) \sqrt{M\epsilon}/\sigma^2$  and  $\gamma = (0.477 \pm 0.005) \epsilon/\sigma^2$  obtained from the MD system (cf. Supplemental Material [45]).

### C. Coalescence of two ridges

As a second test case for the quality of the mapping procedure between the MD and TFE models, we investigated the coalescence of two ridges on a homogeneous substrate. To get an input geometry a ridge on a surface with a wettability of  $\epsilon_w = 0.707 \epsilon$  is equilibrated in a MD simulation. A copy is then translated in the  $x$  direction in such a way that it has a distance of  $0.5 \sigma$  from the primary ridge at the contact line. To maintain the particle density we further extended the MD system (and thus the surface) in the  $x$  direction by a factor of two. From this MD input geometry, we calculated the positions for the liquid-vapor-transition of the two ridges and used this data as an input for the TFE simulations.

The spatial rescaling from the single switch experiments can be employed without further issues. The result of our temporal mapping can be seen in Fig. 7. One can observe that in this case the relation between both models cannot be reasonably fit with a single linear function. Instead, a piecewise linear function is well suited to represent the data. In Fig. 7 the colors of the linear fits match the data points used for fitting. The intersection of the linear functions is at  $t_{\text{MD}} = t_c = 18.1 \times 10^4 \tau$ . Figure 7 visualizes, which times correspond based on our timescale mapping.

In particular, the time  $t_c$  (black dashed line) corresponds to the time at which there is no longer a local minimum in the height profiles, i.e., the time at which the merging process of both droplets is completed. Plots of the height profiles corresponding to the matched times can be found in the Supplemental Material [45]. After  $t_c$  is reached, the droplet still contracts further. The timescale ratios are  $R_{f_{\text{coal},1}} = 3.64 \times 10^4 \tau$  in the first part and  $R_{f_{\text{coal},2}} = 1.71 \times 10^4 \tau$  in the second part.

Note that the value of  $R_{f_{\text{coal},2}} = 1.71 \times 10^4 \tau$  deviates not much from the value of  $2.1 \times 10^4 \tau$  which we observed for a single switch in Table I for the final wettability  $\epsilon_w = 0.707 \epsilon$ . About the significant deviations for  $R_{f_{\text{coal},1}}$  we can only speculate. Possibly, the choice of the mobility in the TFE approach does not fully reflect the processes in the initial coalescence regime. Figure 9 shows that the deviations between the MD and the TF profile are higher for  $t \in [0, t_c]$ , especially for  $x = 0$ . This could indicate that the path in phase space does not agree as well as in the case of a single switch and the disjoining pressure might need improvement.

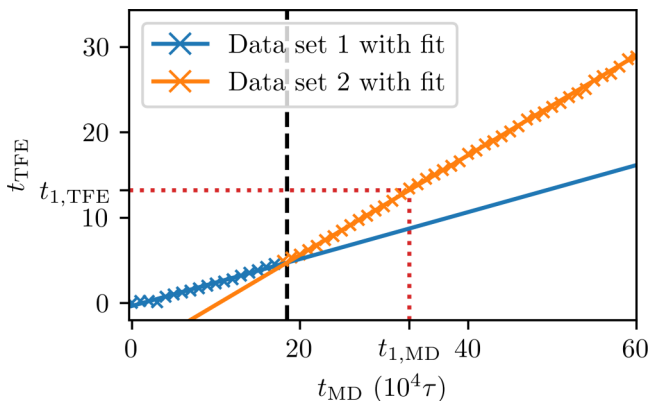


FIG. 7. Result of the temporal mapping for the coalescence of two ridges. Data points of the matched profiles are shown as crosses. Only the crossed data points in matching colors are considered for the corresponding fit shown as a solid line. Two distinct timescales can be observed, both fit with a linear function. The slopes are  $a_1 = (2.64 \pm 0.10) \times 10^{-5} \tau^{-1}$  and  $a_2 = (5.892 \pm 0.030) \times 10^{-5} \tau^{-1}$ . This corresponds to timescale ratios of  $R_{f_{\text{coal},1}} = 3.79 \times 10^4 \tau$  and  $R_{f_{\text{coal},2}} = 1.70 \times 10^4 \tau$ , respectively. The black dashed line marks the intersection of the two linear fits at  $t_{\text{MD}} = t_c = 18.1 \times 10^4 \tau$ .

It is also possible that an initial solution in the TFE model directly taken from the MD model encourages these deviations because the differences in the contact region lead to an initial state in the TFE model, which is farther away from the equilibrium state than the initial state in the MD model. Consequently, the evolution could be artificially accelerated until the droplets have merged. Therefore, we performed additional simulations with initial droplet profiles taken from droplets equilibrated within the TFE model at the same peak distance. However, we essentially obtained the same results.

Again, we can use our mapping approach to check the similarity of both approaches in the space-time plot; see Fig. 8. Furthermore, in Fig. 9 the evolution of the height profile at three distinct points is highlighted. The results match very well except for the anticipated difference at the contact region. Here we have used the strength of our mapping approach that we do not need a simple linear relation between time but can deal with arbitrary monotonic relations.

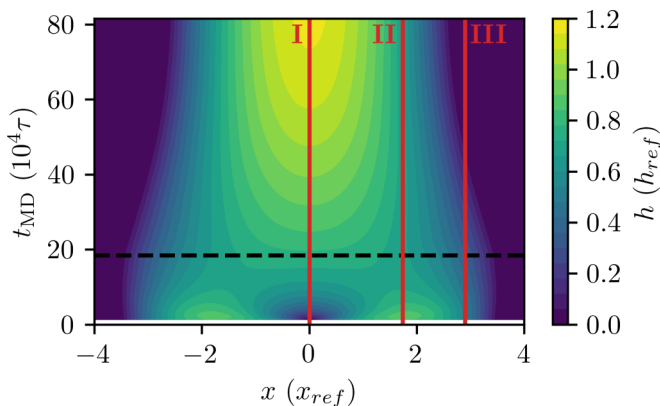


FIG. 8. Space-time plots showing the coalescence of two ridges in the TFE model. The black dashed line is where the TFE timescale is split and the linear fits in Fig. 7 intersect. The height is scaled just as in Sec. III B. The space-time plot for the MD model is omitted because it is very similar to the TFE space-time plot.

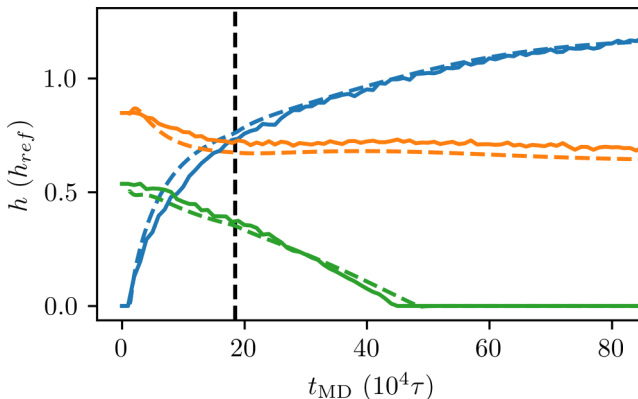


FIG. 9. Three characteristic height profiles along the marked lines I (blue), II (orange), and III (red) as shown in Fig. 8. The height profiles extracted from the MD model are represented with solid lines, whereas the height profiles from the TFE model are dashed. The scaling is the same as in Fig. 8. The dashed vertical line marks the time step, where the scaling factor is changed from  $R_{f_{\text{coal},1}}$  to  $R_{f_{\text{coal},2}}$ .

#### IV. CONCLUSION

In this paper, we have presented a first step toward the quantitative comparison between the microscopic MD and the mesoscopic TFE model for the dynamics of liquid droplets. In a first step, the parameters responsible for the substrate wettability in the respective models are mapped for equilibrium droplets via the rFWHM. Thereby, a mapping between the spatial quantities is achieved. In the second step, the general approach for the mapping of the timescales is based on matching the quantity  $K$ , which depends on the droplet shapes, is applied. The applicability of the presented approach is shown thoroughly for two examples, a droplet on a homogeneous, switchable substrate and the coalescence of two droplets. We have demonstrated that intermediate steps in the evolution are in good agreement. This implies that the same path in phase space is taken in both models. This can be attributed to our reliable mapping of the parameters  $\epsilon_w$  and  $\rho$  responsible for the wettability in their respective models.

Note that our mapping can always be applied, as long as one stays within the limits of the TFE models, i.e., low contact angle and concept of a precursor film. If one keeps the limits in mind, computational resources can be saved, because it enables one to accurately find the parameter range of interest in the TFE model and perform simulations on the mesoscopic scale, while still featuring the same quantitative nonequilibrium time evolution. The other direction is also possible, e.g., some interesting behavior is found within the TFE model and the MD model can provide microscopic insights into the dynamics. The presented approach is not specially tailored to the employed thin-film model. An application of the presented mapping approach for a continuum model, which allows for larger contact angles (e.g., macroscopic boundary element method [25]), is also possible. Mapping to continuum models additionally promises fruitful results with the help of bifurcation analysis, which can help predict onsets of instabilities or explore large parameter spaces systematically along stable branches.

The time mapping for the switching simulations indicates that the resulting mapping does not depend on the initial wettability to a very good approximation. This is indeed a very promising result, confirming the ability of the TFE approach to reproduce the microscopic results. Interestingly, two relevant deviations from a very simple mapping behavior could be observed. First, the factor  $R$  between both timescales slightly depends on the final wettability. Second, in the case of coalescence, we found a nonlinear relation between timescales. These observations suggest that, e.g., the mobility or the disjoining pressure may need to be adapted for an even closer agreement. However, since in our approach the equilibrium properties are fully matched, the deviations are always of order unity.

So far we have chosen a standard choice of mobility and disjoining pressure (cf. [11,13] among others) and we matched the most important characteristics of the disjoining pressure to the MD model, i.e. we made sure, that the minimum of the interface potential was correct, that the precursor film height was chosen adequately, and that the wetting regime was correctly mirrored by our disjoining pressure. In the future, our approach could be extended to a thin-film model with a fine-tuned disjoining pressure. Literature provides ample opportunities to extract the disjoining pressure directly from microscopic models, which enables comparisons between models in the static case [35–38,58–61]. In contrast to the calculation of the disjoining pressure, one needs to consider dynamics to be able to extract information about the mobility from MD models. Here we used a cubic mobility, which can be derived from no-slip boundary conditions. A precise mobility extracted from microscopic models promises to improve the TFE description of a MD model and is the subject of future work. Our procedure could serve as a measure to conclude, whether mobility and disjoining pressure were chosen adequately as you would expect a proportional relation of the timescales in the models.

Furthermore, we would like to stress that in all cases the mapping of the times can be applied in a generic manner. This makes the mapping approach versatile and provides the ability to map timescales if characteristic times or other quantities necessary for a temporal mapping are not easily and reliably accessible.

In the accompanying Zenodo dataset [62], we provide the simulation data, the code to reproduce the figures, and the oomph-lib code to perform the simulations in the TFE model.

#### ACKNOWLEDGMENTS

We wish to acknowledge the financial support by the Deutsche Forschungsgemeinschaft (DFG) via respective Grant No. 422792072 within SPP 2171.

- 
- [1] M. K. Chaudhury and G. M. Whitesides, How to make water run uphill, *Science* **256**, 1539 (1992).
  - [2] H. Gau, S. Herminghaus, P. Lenz, and R. Lipowsky, Electrochemical principles for active control of liquids on submillimeter scales, *Science* **283**, 46 (1999).
  - [3] B. Yoon, H. Acharya, G. Lee, H.-C. Kim, J. Huh, and C. Park, Nanopatterning of thin polymer films by controlled dewetting on a topographic pre-pattern, *Soft Matter* **4**, 1467 (2008).
  - [4] R. Seemann, M. Brinkmann, E. J. Kramer, F. F. Lange, and R. Lipowsky, Wetting morphologies at microstructured surfaces, *Proc. Natl. Acad. Sci. USA* **102**, 1848 (2005).
  - [5] W. Wang, C. Du, C. Wang, M. Hirtz, L. Li, J. Hao, Q. Wu, R. Lu, N. Lu, Y. Wang, H. Fuchs, and L. Chi, High-resolution triple-color patterns based on the liquid behavior of organic molecules, *Small* **7**, 1403 (2011).
  - [6] J. Zhu, M. Wilczek, M. Hirtz, J. Hao, W. Wang, H. Fuchs, S. V. Gurevich, and L. Chi, Branch suppression and orientation control of Langmuir–Blodgett patterning on prestructured surfaces, *Adv. Mater. Interfaces* **3**, 1600478 (2016).
  - [7] K. Kargupta and A. Sharma, Templating of Thin Films Induced by Dewetting on Patterned Surfaces, *Phys. Rev. Lett.* **86**, 4536 (2001).
  - [8] J. Koplik, T. S. Lo, M. Rauscher, and S. Dietrich, Pearling instability of nanoscale fluid flow confined to a chemical channel, *Phys. Fluids* **18**, 032104 (2006).
  - [9] M. Wilczek, J. Zhu, L. Chi, U. Thiele, and S. V. Gurevich, Dip-coating with prestructured substrates: Transfer of simple liquids and Langmuir–Blodgett monolayers, *J. Phys.: Condens. Matter* **29**, 014002 (2017).
  - [10] H. Wang, O. Buller, W. Wang, A. Heuer, D. Zhang, H. Fuchs, and L. Chi, Area confined position control of molecular aggregates, *New J. Phys.* **18**, 053006 (2016).
  - [11] C. Honisch, T.-S. Lin, A. Heuer, U. Thiele, and S. V. Gurevich, Instabilities of layers of deposited molecules on chemically stripe patterned substrates: Ridges versus drops, *Langmuir* **31**, 10618 (2015).



- [12] P. Lenz and R. Lipowsky, Morphological Transitions of Wetting Layers on Structured Surfaces, *Phys. Rev. Lett.* **80**, 1920 (1998).
- [13] W. Tewes, O. Buller, A. Heuer, U. Thiele, and S. V. Gurevich, Comparing kinetic Monte Carlo and thin-film modeling of transversal instabilities of ridges on patterned substrates, *J. Chem. Phys.* **146**, 094704 (2017).
- [14] H. F. Wu, K. A. Fichthorn, and A. Borhan, An atomistic–continuum hybrid scheme for numerical simulation of droplet spreading on a solid surface, *Heat Mass Transfer* **50**, 351 (2014).
- [15] J. Zhang, M. K. Borg, and J. M. Reese, Multiscale simulation of dynamic wetting, *Int. J. Heat Mass Transfer* **115**, 886 (2017).
- [16] R. Wang, K. Hashimoto, A. Fujishima, M. Chikuni, E. Kojima, A. Kitamura, M. Shimohigoshi, and T. Watanabe, Light-induced amphiphilic surfaces, *Nature (London)* **388**, 431 (1997).
- [17] X. Feng, J. Zhai, and L. Jiang, The fabrication and switchable superhydrophobicity of TiO<sub>2</sub> nanorod films, *Angew. Chem., Int. Ed.* **44**, 5115 (2005).
- [18] R.-D. Sun, A. Nakajima, A. Fujishima, T. Watanabe, and K. Hashimoto, Photoinduced surface wettability conversion of ZnO and TiO<sub>2</sub> thin films, *J. Phys. Chem. B* **105**, 1984 (2001).
- [19] K. Ishihara, A. Okazaki, N. Negishi, I. Shinohara, T. Okano, K. Kataoka, and Y. Sakurai, Photo-induced change in wettability and binding ability of azoaromatic polymers, *J. Appl. Polym. Sci.* **27**, 239 (1982).
- [20] R. Rosario, D. Gust, M. Hayes, F. Jahnke, J. Springer, and A. A. Garcia, Photon-modulated wettability changes on spiropyran-coated surfaces, *Langmuir* **18**, 8062 (2002).
- [21] F. Zhu, S. Tan, M. K. Dhinakaran, J. Cheng, and H. Li, The light-driven macroscopic directional motion of a water droplet on an azobenzene-calix[4] arene modified surface, *Chem. Commun.* **56**, 10922 (2020).
- [22] W. Jiang, G. Wang, Y. He, X. Wang, Y. An, Y. Song, and L. Jiang, Photo-switched wettability on an electrostatic self-assembly azobenzene monolayer, *Chem. Commun.* **28**, 3550 (2005).
- [23] J. Groten, C. Bunte, and J. Rühe, Light-induced switching of surfaces at wetting transitions through photoisomerization of polymer monolayers, *Langmuir* **28**, 15038 (2012).
- [24] K. Ichimura, S.-K. Oh, and M. Nakagawa, Light-driven motion of liquids on a photoresponsive surface, *Science* **288**, 1624 (2000).
- [25] J. Grawitter and H. Stark, Steering droplets on substrates using moving steps in wettability, *Soft Matter* **17**, 2454 (2021).
- [26] T. M. Squires and S. R. Quake, Microfluidics: Fluid physics at the nanoliter scale, *Rev. Mod. Phys.* **77**, 977 (2005).
- [27] M. P. Allen and D. J. Tildesley, *Computer Simulation of Liquids*, 2nd ed. (Oxford University Press, Oxford, 2017), p. 640.
- [28] M. J. de Ruijter, T. D. Blake, and J. De Coninck, Dynamic wetting studied by molecular modeling simulations of droplet spreading, *Langmuir* **15**, 7836 (1999).
- [29] J. Roy Choudhuri and P. Nath, Wetting transition of a nanodrop on switchable hydrophilic-hydrophobic surfaces, *Surf. Interfaces* **21**, 100628 (2020).
- [30] A. Oron, S. H. Davis, and S. G. Bankoff, Long-scale evolution of thin liquid films, *Rev. Mod. Phys.* **69**, 931 (1997).
- [31] D. Bonn, J. Eggers, J. Indekeu, J. Meunier, and E. Rolley, Wetting and spreading, *Rev. Mod. Phys.* **81**, 739 (2009).
- [32] U. Thiele, Thin film evolution equations from (evaporating) dewetting liquid layers to epitaxial growth, *J. Phys.: Condens. Matter* **22**, 084019 (2010).
- [33] N. G. Hadjiconstantinou, Combining atomistic and continuum simulations of contact-line motion, *Phys. Rev. E* **59**, 2475 (1999).
- [34] P. G. de Gennes, Wetting: Statics and dynamics, *Rev. Mod. Phys.* **57**, 827 (1985).
- [35] A. P. Hughes, U. Thiele, and A. J. Archer, Influence of the fluid structure on the binding potential: Comparing liquid drop profiles from density functional theory with results from mesoscopic theory, *J. Chem. Phys.* **146**, 064705 (2017).
- [36] N. Tretyakov, M. Müller, D. Todorova, and U. Thiele, Parameter passing between molecular dynamics and continuum models for droplets on solid substrates: The static case, *J. Chem. Phys.* **138**, 064905 (2013).

- [37] A. P. Hughes, U. Thiele, and A. J. Archer, Liquid drops on a surface: Using density functional theory to calculate the binding potential and drop profiles and comparing with results from mesoscopic modelling, *J. Chem. Phys.* **142**, 074702 (2015).
- [38] O. Buller, W. Tewes, A. J. Archer, A. Heuer, U. Thiele, and S. V. Gurevich, Nudged elastic band calculation of the binding potential for liquids at interfaces, *J. Chem. Phys.* **147**, 024701 (2017).
- [39] J. A. Anderson, J. Glaser, and S. C. Glotzer, Hoomd-blue: A python package for high-performance molecular dynamics and hard particle Monte Carlo simulations, *Comput. Mater. Sci.* **173**, 109363 (2020).
- [40] P. J. Hoogerbrugge and J. M. V. A. Koelman, Simulating microscopic hydrodynamic phenomena with dissipative particle dynamics, *Europhys. Lett.* **19**, 155 (1992).
- [41] C. L. Phillips, J. A. Anderson, and S. C. Glotzer, Pseudo-random number generation for Brownian dynamics and dissipative particle dynamics simulations on GPU devices, *J. Comput. Phys.* **230**, 7191 (2011).
- [42] T. Ingebrigtsen and S. Toxvaerd, Contact angles of Lennard-Jones liquids and droplets on planar surfaces, *J. Phys. Chem. C* **111**, 8518 (2007).
- [43] J. H. Weijs, A. Marchand, B. Andreotti, D. Lohse, and J. H. Snoeijer, Origin of line tension for a Lennard-Jones nanodroplet, *Phys. Fluids* **23**, 022001 (2011).
- [44] M. Kanduč, Going beyond the standard line tension: Size-dependent contact angles of water nanodroplets, *J. Chem. Phys.* **147**, 174701 (2017).
- [45] See Supplemental Material at <http://link.aps.org/supplemental/10.1103/PhysRevFluids.8.013902> for additional information and computational details.
- [46] V. S. Mitlin, Dewetting of solid surface: Analogy with spinodal decomposition, *J. Colloid Interface Sci.* **156**, 491 (1993).
- [47] R. Fetzer, K. Jacobs, A. Münch, B. Wagner, and T. P. Witelski, New Slip Regimes and the Shape of Dewetting Thin Liquid Films, *Phys. Rev. Lett.* **95**, 127801 (2005).
- [48] A. Münch, B. Wagner, and T. P. Witelski, Lubrication models with small to large slip lengths, *J. Eng. Math.* **53**, 359 (2005).
- [49] B. Davidovitch, E. Moro, and H. A. Stone, Spreading of Viscous Fluid Drops on a Solid Substrate Assisted by Thermal Fluctuations, *Phys. Rev. Lett.* **95**, 244505 (2005).
- [50] M. Heil and A. L. Hazel, oomph-lib—an object-oriented multi-physics finite-element library, in *Fluid-Structure Interaction*, edited by H.-J. Bungartz and M. Schäfer (Springer, Berlin, Heidelberg, 2006), pp. 19–49.
- [51] D. E. Sullivan, Surface tension and contact angle of a liquid–solid interface, *J. Chem. Phys.* **74**, 2604 (1981).
- [52] R. Pandit, M. Schick, and M. Wortis, Systematics of multilayer adsorption phenomena on attractive substrates, *Phys. Rev. B* **26**, 5112 (1982).
- [53] E. H. Hauge and M. Schick, Continuous and first-order wetting transition from the van der Waals theory of fluids, *Phys. Rev. B* **27**, 4288 (1983).
- [54] S. Dietrich and M. Schick, Critical wetting of surfaces in systems with long-range forces, *Phys. Rev. B* **31**, 4718 (1985).
- [55] S. Dietrich and M. Schick, Order of wetting transitions, *Phys. Rev. B* **33**, 4952 (1986).
- [56] N. Kubochkin and T. Gambaryan-Roisman, Wetting at nanoscale: Effect of surface forces and droplet size, *Phys. Rev. Fluids* **6**, 093603 (2021).
- [57] U. Thiele, Recent advances in and future challenges for mesoscopic hydrodynamic modelling of complex wetting, *Colloids Surf., A* **553**, 487 (2018).
- [58] M. Müller and L. G. lez MacDowell, Wetting of polymer liquids: Monte Carlo simulations and self-consistent field calculations, *J. Phys.: Condens. Matter* **15**, R609 (2003).
- [59] V. P. Carey and A. P. Wemhoff, Disjoining pressure effects in ultra-thin liquid films in micropassages—comparison of thermodynamic theory with predictions of molecular dynamics simulations, *J. Heat Transfer* **128**, 1276 (2006).
- [60] L. MacDowell, Computer simulation of interface potentials: Towards a first principle description of complex interfaces? *Eur. Phys. J. Spec. Top.* **197**, 131 (2011).

- [61] D. N. Sibley, P. Llombart, E. G. Noya, A. J. Archer, and L. G. MacDowell, How ice grows from premelting films and water droplets, *Nat. Commun.* **12**, 239 (2021).
- [62] M. Stieneker, L. Topp, S. Gurevich, and A. Heuer, Data supplement for “Multiscale perspective on wetting on switchable substrates: Mapping between microscopic and mesoscopic models,” data set on Zenodo (2021); <http://doi.org/10.5281/zenodo.5147918>.